metals

MDPI

Article

The Low-Cycle Fatigue Performance of Emerging Titanium Alloys for Aeroengine Applications

Peter Davies [1,*], Sean John [1], Helen Davies [1], Martin Bache [1], Kate Fox [2], Christopher Collins [2], Nigel Martin [2] and Rebecca Sandala [2]

[1] Institute of Structural Materials, Swansea University, Bay Campus, Fabian Way, Crymlyn Burrows, Swansea SA1 8EN, UK
[2] Rolls-Royce plc, P.O. Box 31, Derby DE24 8BJ, UK
* Correspondence: p.d.davies@swansea.ac.uk; Tel.: +44-1792604382

Abstract

The low-cycle fatigue behavior of three titanium alloys (including two wrought alloys that are commercially available and one under development via a powder sintering technique) is described in order to assess the relative capabilities of a fourth, novel proprietary alloy, designated as RR11. Despite relatively increased levels of beta stabilization, each alloy remains within the general alpha–beta microstructural category and could be considered as an engineering alternative to the well-established Ti-6Al-4V. The relationships between fatigue behavior, microstructure, grain morphology, micro-texture, and alloy chemistry are explored. Emphasis is placed upon the potential cold dwell fatigue sensitivity of the four alternative alloys, which is particularly pertinent since it was recognized that Ti-6Al-4V can suffer from cold dwell-related behavior subject to selected thermo-mechanical processing.

Keywords: titanium alloys; low-cycle fatigue; dwell fatigue; micro-textured regions; microstructure

Academic Editor: Eiichi Sato

Received: 11 July 2025
Revised: 14 November 2025
Accepted: 15 November 2025
Published: 20 November 2025

Citation: Davies, P.; John, S.; Davies, H.; Bache, M.; Fox, K.; Collins, C.; Martin, N.; Sandala, R. The Low-Cycle Fatigue Performance of Emerging Titanium Alloys for Aeroengine Applications. *Metals* **2025**, *15*, 1274. https://doi.org/10.3390/met15111274

1. Introduction

The global development of titanium alloys has been closely tied to the evolving demands of the aerospace industry. Their high strength-to-weight ratio across ambient to intermediate temperatures has enabled their widespread use in aeroengine components, including compressors, containment structures, and fan assemblies [1]. More recently, titanium alloys have also been employed in the manufacture of integrally bladed discs (blisks) [2]. In such applications, alpha–beta (α/β) titanium alloys are typically used, as their dual-phase microstructures can be tailored through thermo-mechanical processing to meet specific performance requirements. The resulting microstructure, together with the crystallographic texture, has a critical influence on the mechanical behavior [3–5].

Among these alloys, Ti-6Al-4V (Ti-6-4) remains a cornerstone of aeroengine design, owing to its balance of strength, fatigue resistance, and formability. Specific microstructures can be manipulated through various processing routes, making it highly adaptable for different applications. However, as performance requirements in modern engines increase, the mechanical capabilities of existing alloys, including Ti-6-4, must also evolve, particularly in relation to fatigue resistance under complex loading conditions.

One persistent concern for titanium alloy components is their susceptibility to cold dwell fatigue, particularly when operating under high mean stress conditions in rotating

parts such as compressor discs [6]. This issue first emerged in the 1970s following failures involving near-α alloys such as Ti–6Al–5Zr–0.5Mo–0.25Si (IMI 685), prompting the shift towards the α/β alloy Ti-6-4 [6]. The relatively finer grain size of Ti-6-4, when compared to near-α alloys such as Ti-5.5Al-3.5Sn-3Zr-1Nb-0.25Mo-0.3Si (Ti-829) and Ti-6Al-5Zr-0.5-Mo-0.25Si (Ti-685), was thought to alleviate the extent of planar slip [7,8]. However, selected studies from the late 1980s onwards revealed that Ti-6-4 could also exhibit dwell sensitivity, particularly when coarse lamellar microstructures were present [9].

More recently, comprehensive research investigations [10,11] have demonstrated that Ti-6-4 is also dwell-sensitive when processed into a bimodal microstructure subject to the presence of micro-textured regions (MTRs), clusters of α-phase grains with a common crystallographic orientation. Identified through the early adoption of electron backscattered diffraction (EBSD) techniques [12], MTRs act as single, effective structural units (ESUs) during fatigue loading [13], increasing continuous slip plane lengths, promoting crack initiation, and facilitating accelerated crack growth [14]. The role of the transformed β phase is also important in bimodal microstructures, since the finer scaled, secondary α phase evolved within may inherit orientations that align with the primary α phase due to Burgers orientation relationships (BORs) [15]. The presence, size, and intensity of MTRs are highly dependent on the thermo-mechanical processing route [16].

The dwell fatigue mechanism, involving a sequence of dislocation pile-up at barriers such as grain or phase boundaries, followed by stress redistribution (commonly referred to as load shedding), is time-dependent and exacerbated by extended periods of loading at relatively high stress. This phenomenon causes "weak" grains (those where the c-axis of the hexagonal α phase is inclined to the applied stress) to transfer stress to neighboring "strong" grains, which would normally be considered less favorably oriented for slip on the basal plane (i.e., their c-axis is parallel to the applied stress) [17]. As a result, slip and crack initiation can occur in the strong grain, on or close to the basal {0001} plane [18] and oriented nearly perpendicular to the principal applied tensile stress axis. These effects are particularly pronounced in bimodal α/β microstructures, where the dislocation activity is only partially hindered by phase boundaries [16]. Fractography demonstrates that dwell-related fatigue failures are often associated with the presence of quasi-cleavage facets, which initiate on the basal plane of individual primary α grains [18]. It must be emphasized, however, that dwell failure and faceting are not an exclusive relationship. Facets are a naturally occurring feature of all near-α and α/β titanium alloys subjected to fatigue conditions, irrespective of the loading waveform. They are even formed under static, time-dependent creep loading at ambient temperatures.

Beyond Ti-6-4, other well-established alloys, such as Ti-5.8Al-4.0Sn-3.5Zr-0.7Nb-0.5Mo-0.35Si (Ti-834) [19] and Ti-6Al-2Sn-4Zr-2Mo (Ti-6242) [20], have also shown dwell sensitivity when employed in specific microstructural states. Conversely, more recent alloys, like Ti-6Al-2Sn-4Zr-6Mo (Ti-6246) [21], Ti-3.9V-0.85Al-0.25Si-0.25Fe (Ti-407) [22,23], and Ti-5.3Al-7.7V-0.5Si-0.25Fe-0.18O (Ti-575) [24–26], have demonstrated greater resistance to dwell fatigue through precise thermo-mechanical processing, chemistry, and microstructure control. The formation of MTRs and their effect on fatigue performance remain strongly influenced by factors such as β-stabilizing elements, billet processing, forging steps, and final heat treatment [16].

Our recent interest has focused upon a range of α/β titanium alloys that offer various processing and/or mechanical property improvements relative to Ti-6-4. One line of investigation has been to evaluate the effect of increased β-phase stabilization, improving the hot working characteristics via a reduction in the β transus temperature and ultimately eliminating the formation of MTRs where possible.

One outcome of this research has been the development of a novel proprietary alloy (designated as RR11), currently under patent application [27]. The present paper will specifically demonstrate the fatigue capability of RR11 under low-cycle fatigue (LCF) and dwell waveform conditions. Data will be compared to two relatively new, cast and wrought α/β alloys that also offer greater β stabilization. Subject to commercial sensitivity, these alloys are simply referred to as Alloy A and Alloy B, however, both were melted and processed on an industrial scale. In addition, comparisons will also be made to alloy Ti–5.5Al–4.5V–2.5Mo–1.5Cr. (S23) [28], a contemporary developmental alloy that was processed via a powder route, i.e., Field-Assisted Sintering Technology (FAST). The current findings should provide a basis for further forms of experimentation and potential alloy down-selection in the future.

2. Experimental

Fatigue data were generated under room-temperature LCF and dwell LCF loading conditions using four different alloys.

2.1. Alloy Chemistry

The precise chemical composition of S23 is available in previous studies [28–30]. Compared to Ti-6-4, each alloy contains a higher proportion of β-stabilizing elements, although they remain under the general α/β classification. Unfortunately, we are unable to release the full compositional details of alloys A and B or those of the novel RR11 alloy while it remains under patent application. Instead, the total aluminum equivalent content (i.e., % of alpha-stabilizing elements) and molybdenum equivalent (beta stabilizers) in the four alloys under mechanical assessment are illustrated in Figure 1 and compared to Ti-6-4. Notably, Alloy B offers the highest α stabilization. RR11 contains relatively low levels of α-stabilizing elements.

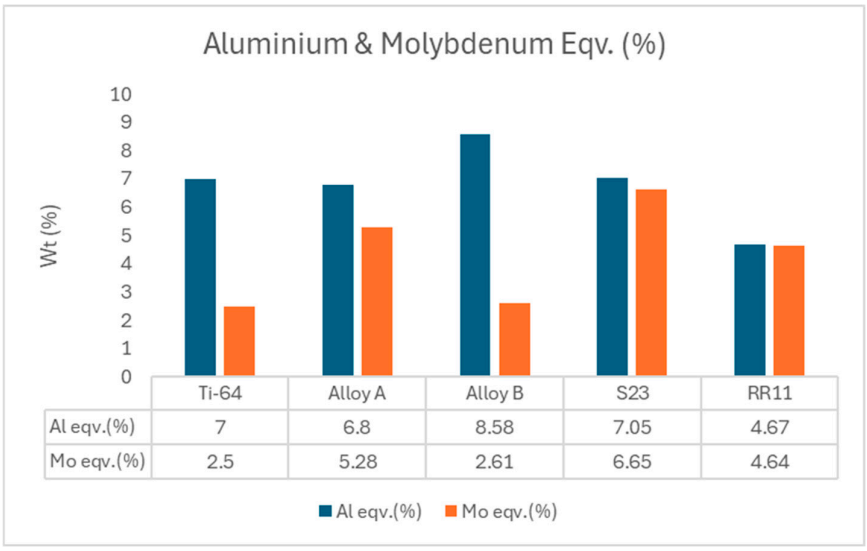

Figure 1. Aluminum and molybdenum equivalent contents of Ti-6-4, adapted from [29] compared to the four alloys under evaluation.

2.2. Material Processing

Alloy A was vacuum arc remelted–vacuum arc remelted (VAR-VAR) and then thermo-mechanically worked down to a 100 mm diameter bar and cut to 300 mm in length. Bars were hammer-forged (parallel to the longitudinal axis) at 885 °C. The subsequent pancakes were then solution heat-treated at 885 °C for 1 h and water quenched before being annealed at 700 °C for 2 h and air-cooled to room temperature.

Alloy B was plasma arc remelted (PAM)-VAR and thermo-mechanically worked down to a 100 mm diameter bar and cut to bars of 300 mm in length. Bars were forged (parallel to the longitudinal axis) at 900 °C. A final heat treatment at 760 °C for 2 h was applied, followed by air cooling.

A disc of S23, 250 mm diameter × 20 mm thickness, was produced via the FAST sintering process, combining a blend of Ti-6-4 and Ti-5553 powders [28]. Consolidation was performed at 1200 °C for 60 min. An initial heating rate of 50 °C/min was used and then reduced to 25 °C/min for the last 150 °C to avoid overshoot. The alloy was then slow-cooled at a cooling rate of 10 °C/min above the β transus.

RR11 was induction skull melted (ISM) and centrifugally cast (CF) into 60 mm diameter molds. The ingots were then cut into semi-circular profile bars and then flat-rolled at 860 °C. These were then heat-treated at 860 °C for 6 h and cooled to room temperature using vermiculite cooling. The bars were aged at 600 °C for 2 h and cooled to room temperature using vermiculite cooling.

The microstructures of each alloy are illustrated in Figure 2, with the various thermo-mechanical processes (relative to the alloy-specific β transus temperature) illustrated schematically in Figure 3.

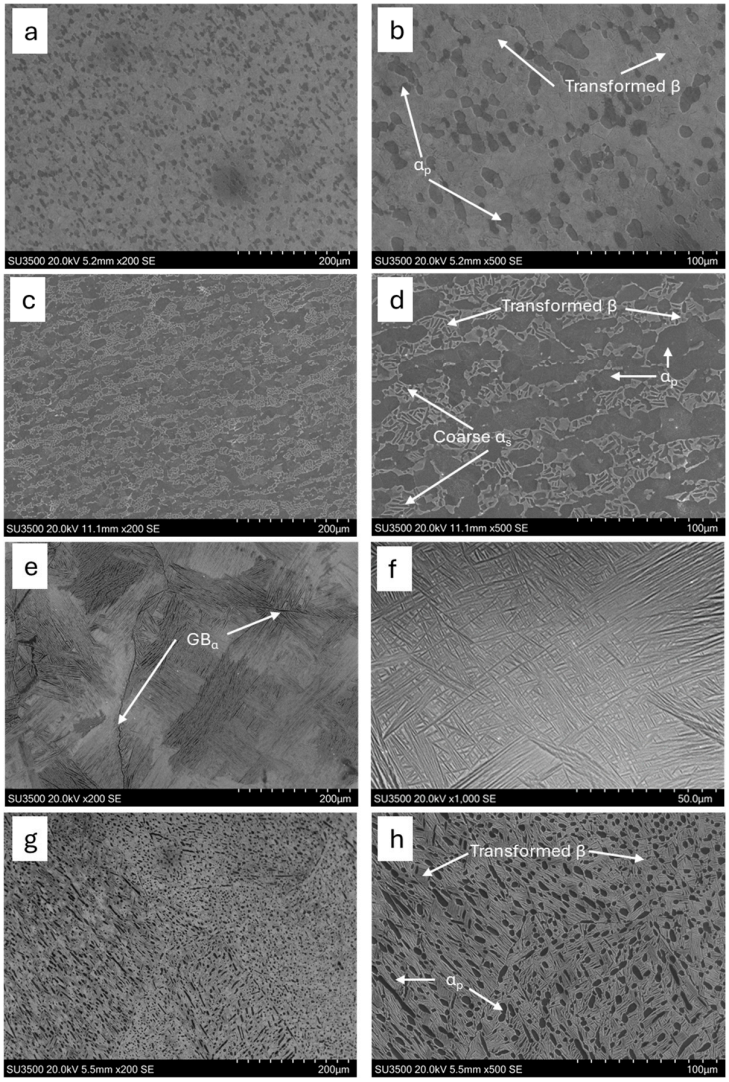

Figure 2. Microstructures: (**a**,**b**) Alloy A, (**c**,**d**) Alloy B, (**e**,**f**) S23, and (**g**,**h**) RR11.

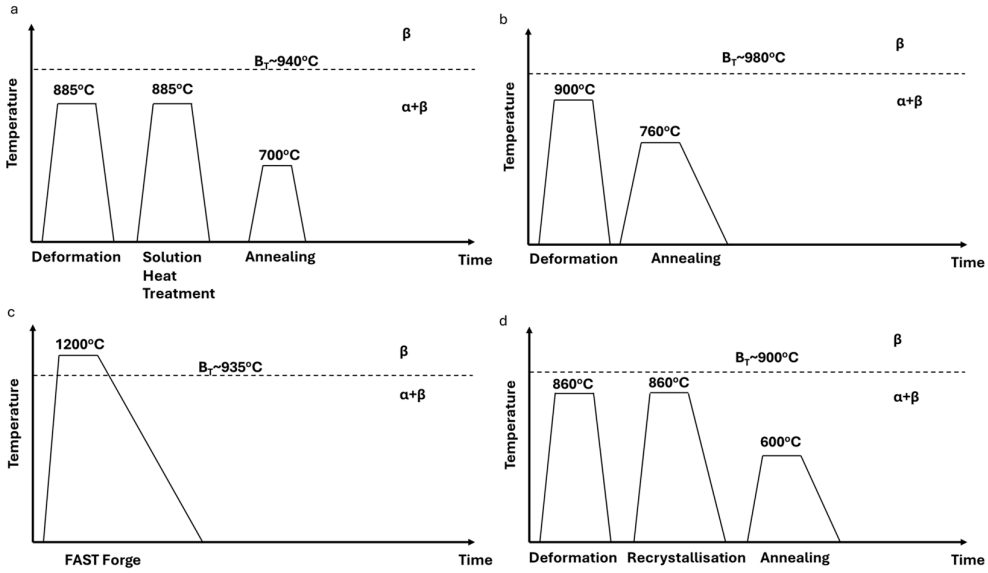

Figure 3. Illustration of the primary processing routes for (**a**) Alloy A, (**b**) Alloy B, (**c**) S23, and (**d**) RR11.

2.3. Microscopy and Electron Backscatter Diffraction

Imaging, EBSD, and energy-dispersive X-ray (EDX) analyses were performed on a Hitachi SU3500 scanning electron microscope in conjunction with AZtec HKL version 5.1 software.

2.4. Mechanical Testing

Cylindrical test specimens, as shown in Figure 4a, were employed for monotonic tensile testing, while the geometry shown in Figure 4b was used for all LCF and dwell cycle fatigue testing (DLCF). Alloy A and Alloy B specimens were taken from forged pancakes, with their longitudinal axis taken from either the original bar stock longitudinal axis or the transverse direction. RR11 specimens were taken from a unidirectionally (UD) rolled plate in the longitudinal direction. The S23 specimens were extracted in a radial orientation relative to the flat disc.

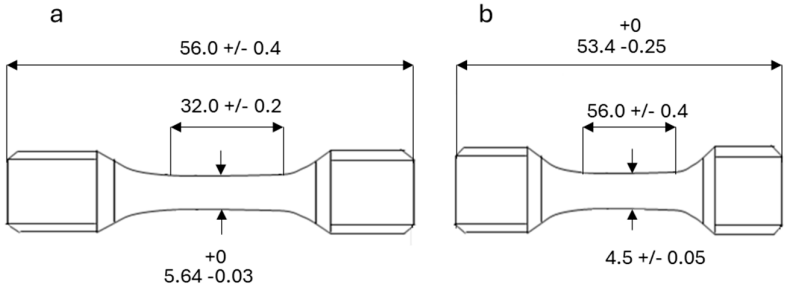

Figure 4. (**a**) Tensile and (**b**) fatigue specimens employed for mechanical testing.

All room-temperature tensile tests were performed in accordance with BS EN 2002-1:2005 [30]. All LCF and DLCF tests, performed in accordance with ISO 1099:2006 [31], were conducted at room temperature under load control and an R ratio of 0.1. The LCF waveform comprised a 1 s linear rising ramp, 1 s hold at peak load, 1 s linear off-load, and 1 s hold at minimum load (i.e., a 1-1-1-1 trapezoidal waveform). All DLCF tests also employed a trapezoidal waveform but encompassed a 60 s hold at peak load (1-60-1-1 trapezoidal waveform). Due to limitations in the volume of material available, only a limited number of specimens were available for testing. Hence, specific applied peak

stresses were targeted (based on the % of yield stress and prior laboratory experience), where it was expected that dwell debits would be exhibited if an alloy was susceptible.

3. Results

3.1. Microstructure

Determining the average grain size in this class of alloy can be difficult due to the variable morphologies resulting from the thermo-mechanical processing route applied. The mean linear intercept (MLI) method was used to determine the average grain size in this study. The MLI was determined by counting the number of grain boundaries that intercepted a straight line or the number of lines of known length. Approximately 100 grain boundaries were sampled for each alloy in order to gain an accurate representation of the average grain size. A comparison of key microstructural features is tabulated in Table 1.

Table 1. A comparison of key microstructural features.

	Microstructural Features				
Alloy	**Microstructure Description**	**Average Prior β Grain Size (μm)**	**Average Primary α Grain Size (μm)**	**Average Primary α Content (%)**	**Grain Boundary α**
Alloy A	Bimodal	-	13	24	Yes
Alloy B	Bimodal	-	13.5	43	No
S23	Lamellar	510	-	-	Yes
RR11	Bimodal	>500	6	24	No

Alloy A displayed a bimodal microstructure, with primary α grains contained in a transformed β matrix (Figure 2a,b). The alloy was found to have an average primary α grain size of ~13 μm in diameter and a primary α content of ~24%. The microstructure often illustrated regions of continuous grain boundary α (GB_α) (Figure 2b).

Alloy B also displayed a bimodal microstructure; however, primary α particles often coalesced (Figure 2c,d). The alloy had an average primary α grain size of ~13.5 μm in diameter and a primary α content of ~43%. The transformed β product contained relatively coarse secondary α, often several microns wide (Figure 2d).

S23 displayed an equiaxed lamellar microstructure (Figure 2e,f) with an average prior β grain size of ~510 μm in diameter. The prior β grains were typically, but not always, decorated with GB_α several microns in width. While the internal structure of these grains usually consisted of packets of aligned laths, occasionally, areas of fine basketweave structure (~100–300 μm in diameter) were observed (Figure 2f).

RR11 displayed a bimodal microstructure, with primary α grains contained in a transformed β matrix (Figure 2g,h). The alloy demonstrated the greatest level of grain refinement, with an average primary α grain size of ~6 μm in diameter and a primary α content of ~24%. The primary α grains were often found to be elongated (Figure 2h).

3.2. Microtexture

Inverse pole figure (IPF) maps and pole figures for all four alloys are illustrated in Figure 5a–d. Both Alloy A (Figure 5a) and RR11 (Figure 5d) displayed notable texture intensities of 5.8 and 7.4 times random, respectively. Texture intensities of 6.3 times random were measured in selected samples of S23 (Figure 5c); however, these were invariably related to packets of commonly oriented primary α laths within individual grains. Alloy B (Figure 5b) displayed the lowest texture intensity at 1.7 times random.

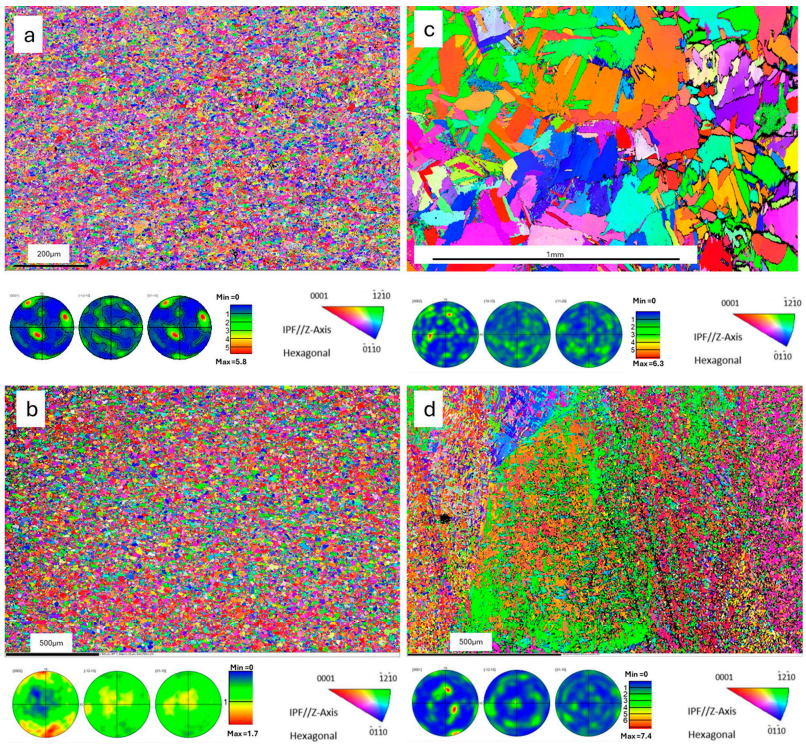

Figure 5. EBSD-derived IPF//Z and pole figures for (**a**) Alloy A, (**b**) Alloy B, (**c**) S23, and (**d**) RR11.

3.3. Monotonic Tensile Testing

Key parameters measured from the room temperature tensile tests are included in Table 2. The results illustrate that Alloy A was the strongest of the four alloys assessed, with an ultimate tensile strength (UTS) of 1111 MPa and 0.2% proof stress of 1027 MPa. This represents an increase in strength of ~5% over the nearest competitor (Alloy B) while also providing excellent ductility when compared to typical Ti-6-4 rolled plate products [32]. While the novel RR11 alloy illustrated relatively low UTS and proof strength, it was clearly the most ductile, surpassing 18% elongation at fracture.

Table 2. Monotonic tensile results.

Alloy	Room-Temperature Monotonic Tensile Properties			
	Modulus (GPa)	**UTS (MPa)**	**0.2% Proof Stress (MPa)**	**Elongation at Fracture (%)**
Alloy A	113	1111	1027	15
Alloy B	112	1053	986	9.7
S23	107	1036	911	7.5
RR11	111	890	776	18.2

3.4. Low-Cycle Fatigue and Dwell Cycle Fatigue

Cyclic and dwell fatigue data for the four alloys are combined as a single SN plot (Figure 6). The absolute peak value of fatigue stress as applied to the individual specimens is employed as the stress criterion. Selected logarithmic trendlines are superimposed to emphasize the differences between alloy strengths and dwell performance. The longest LCF test was terminated as a run-out test at 200,000 cycles, while DLCF tests were restricted to a maximum life of 30,000 cycles due to time restrictions for the test rigs.

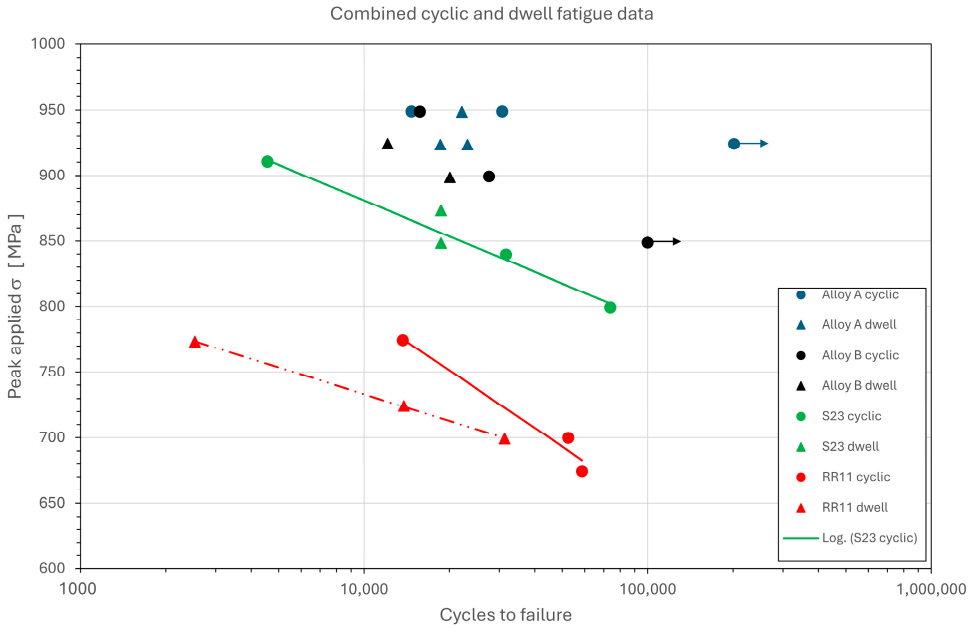

Figure 6. Cyclic and dwell fatigue data measured from the four alloys.

Allowing for the limited number of points per dataset, it is apparent that the two commercial alloys, Alloy A and Alloy B, demonstrated superior LCF strengths. Both indicated a moderate sensitivity to dwell loading. By comparison, the sintered S23 offered a weaker performance, consistent with the larger grain size of this alloy. Notably, however, S23 did not display dwell sensitivity. A single best-fit trend line was superimposed on the combined S23 cyclic data. In turn, when compared to this, the RR11 alloy under similar cyclic LCF loading offers a knockdown in strength by approximately 100 MPa, commensurate with the differences in ultimate static strength listed in Table 2. Separate best-fit lines drawn through the RR11 data help to emphasize the dwell sensitivity of this alloy in its current form. Extrapolation of the best fit through the dwell data points indicates that they would merge with the cyclic LCF performance at approximately 680 MPa (~0.75% of UTS) and a life of 60,000 cycles.

3.5. Fractography

The location of crack initiation was identified in each failed specimen. The spatial locations are shown in Table 3, categorized into three groups: surface (depth of 0–30 μm below the specimen surface, i.e., approximately the diameter of a single primary α grain in the bimodal alloys), near-surface (depths ranging between 30 μm and 300 μm), and sub-surface (depth > 300 μm).

Table 3. Locations and morphology of fatigue crack initiation (by number of specimens).

Alloy		Initiation Site Location			Initiation Site Morphology			
	Test Type	Surface	Near-Surface	Sub-Surface	Colony Cluster	Isolated Colonies	Primary Alpha Clusters	Isolated Primary Alpha
Alloy A	LCF	-	2	-	-	-	-	2
	DLCF	-	3	-	-	-	-	3
Alloy B	LCF	1	2	1	-	-	2	2
	DLCF	-	2	-	-	-	1	1
S23	LCF	2	1	-	3	-	-	-
	DLCF	2	-	-	2	-	-	-
RR11	LCF	-	3	-	-	-	-	3
	DLCF	-	2	1	-	-	-	3

All S23 fatigue failures were distinct from their bimodal counterparts, in that crack initiation was invariably located at surface or near-surface regions, each initiating from clusters of aligned colony grains, irrespective of the cyclic or dwell waveform (Figure 7a).

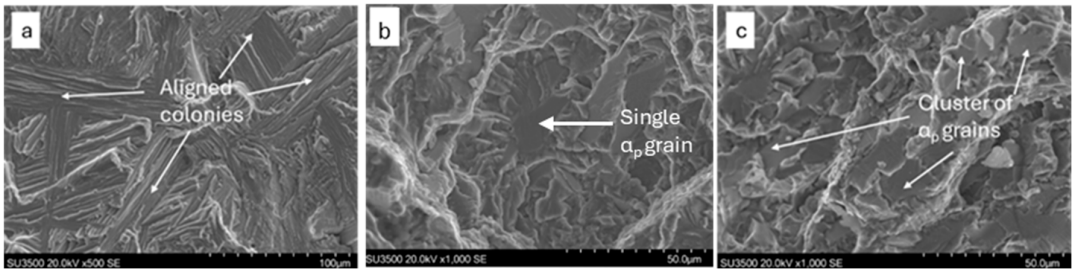

Figure 7. Exemplars of crack initiation: (**a**) from radiating aligned lath colonies in S23, (**b**) isolated facets in Alloy B, and (**c**) clustered facets in Alloy B.

Each of the three bimodal alloys illustrated examples of quasi-cleavage facets, irrespective of the cyclic or dwell waveform. Alloy B appeared to illustrate some of the best examples, either constrained by a single primary α grain (Figure 7b) or often traversing a cluster of juxtaposed primary α grains (Figure 7c).

All Alloy A failures originated near the surface, with each initiating from isolated primary α grains. Fractures in the RR11 specimens initiated near the surface or, most notably, the sub-surface, but again, they initiated from isolated primary α grains.

4. Discussion

When considering the relative mechanical performance displayed by the four different alloys, it should be recognized that two of the variants (namely, Alloy A and Alloy B) are established commercial materials that are produced on an industrial scale. Therefore, their alloy chemistry is fixed, and various thermo-mechanical processing routes are assessed whilst aiming towards specific mechanical attributes. In contrast, the two novel alternatives (S23 and, in particular, RR11) remain in their early stages of development, and the materials supplied for this study were experimental in scale.

Based on absolute fatigue performance alone (Figure 6), the two commercial products provided the greatest strengths, with Alloy A offering superior performance. This is consistent with their respective static properties, whether represented by monotonic yield or ultimate strength (Table 2). Indeed, an identical order of ranking for monotonic and fatigue strength was established across the four alloys evaluated, in the following order:

(Strongest) Alloy A > Alloy B > S23 > RR11

Both Alloy A and Alloy B were processed into a bimodal microstructure with a similar refined primary α grain size, approximating 13 μm in diameter. However, there was a notable difference between the stabilization fractions; with Alloy B containing a high level of aluminum equivalent species, leading to almost double the primary α volume compared to Alloy A. In addition, the secondary α grains in the Alloy B microstructure were coarser. In contrast, Alloy A contained significantly higher volumes of transformed β due to a significantly greater β-stabilized chemistry, with a molybdenum equivalent of 5.28 compared to 2.61 in Alloy B. The β matrix ultimately gives Alloy A its strength and LCF improvement over Alloy B.

A similar knockdown in fatigue performance due to the imposition of dwell loading was measured in both Alloy A and Alloy B, although, admittedly, defining clear best-fit trend lines through the specific cyclic and dwell datasets was made difficult by the limited number of available specimens and inherent scatter in performance. Increasing

the amount of data for these two alloys is an essential requirement during future testing campaigns. Even though greater volume fractions of primary α have previously been shown to make titanium alloys more susceptible to dwell debit [14], on this occasion, it did not appear to adversely affect Alloy B, possibly aided by the relatively low texture intensity of 1.7 times random.

Although dwell sensitivity was detected in both alloys under fatigue regimes previously described as being "relevant to engineering applications" (i.e., $N_f > 10^4$ cycles) [33], the levels of applied peak stress necessary to induce the effect were relatively high, exceeding 85% of the UTS alloy in each case. Similar findings have been reported by this laboratory in relation to the more established metastable β alloy Ti-6246 when processed in various forms [21]. Three different Ti-6246 microstructures were evaluated, considered to represent extreme exemplars resulting from typical forging operations. Each variant required peak stress levels to exceed 90% of static UTS before any indications of dwell sensitivity were detected. This offers reassurance that any consequences of dwell sensitivity could be averted in the current high-strength α/β alloys or metastable β alloys in general through careful component design and the setting of safe stress operating limits and duty cycles.

Compared to the combined fatigue data representing Alloy A and Alloy B, RR11 illustrates a reduction in fatigue strength by approximately 200 MPa. The latter also appears to demonstrate a similar degree of dwell sensitivity (with the effect perhaps over-emphasized in this case by the dwell test performed at 775 MPa, which achieved ~2500 cycles prior to failure). Despite also containing a bimodal microstructure, RR11 notably demonstrated the highest degree of micro-texture at 7.4 times random. Although measurement of the prior β grain size in RR11 was difficult, grains exceeding 500 µm in diameter were sometimes indicated (Figure 5d). In addition, Figure 5d illustrates that packets of primary and secondary α-phase material occasionally congregated at prior β grain boundaries, which themselves formed relatively large MTRs. Together, these two microstructural factors may account for the weaker response from RR11 under both monotonic and fatigue loading.

It is interesting to note that when the fatigue data for Alloy A, Alloy B, and RR11 are replotted employing a normalized criterion (i.e., applied peak stress expressed as a % of UTS for the respective alloy), the performance of the three alloys illustrates a closer correlation, especially towards the short-life end of the SN curve (Figure 8). All three alloys initiated fatigue cracking via the same mechanism, i.e., stress redistribution acting upon primary α grains leading to quasi-cleavage facet formation. Since the primary α grain size was the greatest in the Alloy B material, this alloy illustrated the clearest forms of faceting (Figure 7b), with localized facet clusters corresponding to juxtaposed primary α grains resulting from the elevated α volume fraction (Figure 7c). It has been previously demonstrated that fracture morphology is influenced by micro-texture [34]. MTRs that have their c-axis texture component parallel to the applied stress have been found responsible for highly faceted fracture morphologies, where early-stage crack growth is believed to occur with less resistance [35].

In many ways, the S23 alloy should be considered in isolation. This was the only alloy to be processed via a powder/sinter technique. Although this specific blend composition remains within the α/β classification, at 6.65% molybdenum equivalence, S23 had the closest composition to a metastable β material under the current characterization. The microstructure comprised a relatively large grain size, containing a distribution of basketweave or aligned α laths rather than equiaxed primary α sub-grains. Together with the increased β-phase material, this would encourage multiple slip systems to operate across extensive slip lengths. This would circumvent the planar, basal slip-dominated

mechanisms that control LCF fracture in α/β and near-α alloys [36]. This was evidenced by a lack of quasi-cleavage facets when inspecting S23 fractures. Instead, crack initiation zones were characterized by rough, trans-granular regions exposing the traces of the underlying, radiating lath structures (Figure 7a).

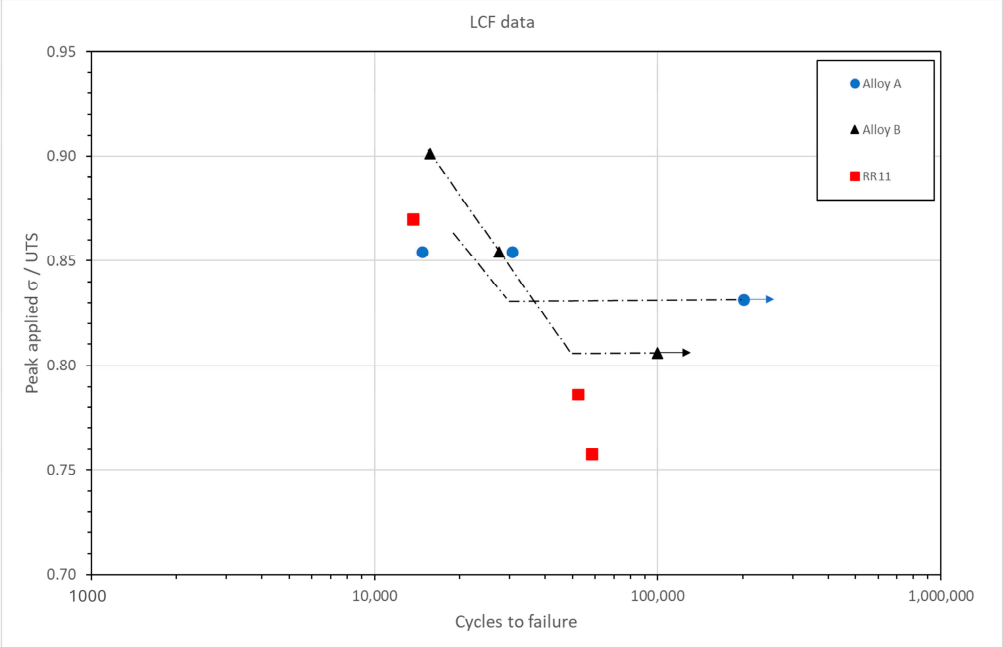

Figure 8. LCF data for Alloy A, Alloy B, and RR11 plotted on the basis of normalized applied peak stress.

Regardless, the S23 alloy displayed relatively good fatigue strength and, most notably, appeared to be insensitive to dwell loading. Despite this promising performance, further development of this alloy can now be considered, including minor changes to the elemental powder blend or thermo-mechanical process, with the latter focused on evolving a bimodal, rather than lath, microstructure.

While the present paper focused on static and LCF properties, it is emphasized that other attributes must be considered before potential selection for engineering applications. For example, the ability to forge and weld all of these alloys of interest has also been central to alloy design. Other pertinent characteristics of fatigue performance are currently under investigation, including high-cycle fatigue (HCF) performance and the influence of mean stress (i.e., Goodman/Haigh relationships). Although HCF research is still at an early stage, RR11 has demonstrated relatively good properties under such circumstances [37]. Further modifications to the RR11 composition and/or associated thermo-mechanical processing could also be considered to improve the fundamental static and fatigue strength of this alloy.

5. Conclusions

Four α/β titanium alloys, each considered as a potential alternative to the widely employed Ti-6-4, were assessed for static, LCF, and DLCF performance.

Two alloys previously developed at a commercial stage, namely, Alloy A and Alloy B, offered the highest static and fatigue strengths when processed into a bimodal microstructure. Both displayed a moderate sensitivity to dwell loading.

A novel, proprietary alloy, RR11, shared many microstructural attributes with Alloy A and Alloy B. However, in terms of absolute stress, both static and fatigue strengths were relatively low in RR11. The elimination of large prior β grains, remnant from thermo-

mechanical processing and containing localized regions of high texture intensity, could offer a route to improve the mechanical properties of this alloy.

The S23 alloy, produced via the FAST powder/sinter process, offered a distinct product form in comparison to the other three wrought materials. S23 displayed intermediate static and fatigue strengths, which could be optimized further through different powder blending and/or thermo-mechanical processing. Crucially, the large grain and heavily β-stabilized lath microstructure helped to overcome dwell sensitivity.

Additional forms of mechanical assessment, to include high-cycle fatigue and range-mean characterization, will be reported in a future publication.

Author Contributions: Conceptualization, P.D., H.D., C.C., N.M., K.F. and R.S.; methodology, P.D., C.C., N.M., K.F. and R.S.; validation, P.D., S.J. and H.D.; formal analysis, P.D., S.J. and M.B.; investigation, P.D. and S.J.; data curation, P.D.; writing—original draft preparation, P.D.; writing—review and editing, P.D., H.D., C.C., N.M., K.F., R.S. and M.B.; resources, C.C., N.M., K.F. and R.S.; project administration, H.D.; funding acquisition, H.D. All authors have read and agreed to the published version of the manuscript.

Funding: This research was funded by the Aerospace Technology Institute (ATI) BETA project—application number: 10052028.

Data Availability Statement: The original contributions presented in this study are included in the article. Further inquiries can be directed to the corresponding author.

Acknowledgments: The provision of materials from Rolls-Royce plc is gratefully acknowledged. Fatigue tests were performed at Swansea Materials Research and Testing Ltd. (SMaRT).

Conflicts of Interest: Authors Kate Fox, Christopher Collins, Nigel Martin and Rebecca Sandala were employed by the company Rolls-Royce plc at the time of writing. The remaining authors declare that the research was conducted in the absence of any commercial or financial relationships that could be construed as a potential conflict of interest.

References

1. Peters, M.; Kumpfert, J.; Ward, C.H.; Leyens, C. Titanium alloys for aerospace applications. *Adv. Eng. Mater.* **2003**, *5*, 419–427. [CrossRef]
2. García, A.M.M. BLISK Fabrication by Linear Friction Welding. In *Advances in Gas Turbine Technology*; IntechOpen: Rijeka, Croatia, 2011; pp. 411–435. [CrossRef]
3. Lütjering, G. Influence of processing on microstructure and mechanical properties of (α + β) titanium alloys. *Mater. Sci. Eng. A* **1998**, *243*, 32–45. [CrossRef]
4. Whittaker, M.T.; Evans, W.J.; Lancaster, R.; Harrison, W.; Webster, P.S. The effect of microstructure and texture on mechanical properties of Ti6-4. *Int. J. Fatigue* **2009**, *31*, 2022–2030. [CrossRef]
5. Peters, G.L.M.; Gysler, A. Influence of texture on fatigue properties of Ti-6Al-4V. *Metall. Mater. Trans. A* **1984**, *15*, 1597–1605. [CrossRef]
6. Bache, M. A review of dwell sensitive fatigue in titanium alloys: The role of microstructure, texture and operating conditions. *Int. J. Fatigue* **2003**, *25*, 1079–1087. [CrossRef]
7. Song, D.W.H.Z. Size effect on the fatigue behaviour of IMI 829 titanium alloy under dwell conditions. *Int. J. Fatigue* **1989**, *11*, 85–90. [CrossRef]
8. Wojcik, C.C.; Chan, K.S.; Koss, D.A. Stage I fatigue crack propagation in a titanium alloy. *Acta Metall.* **1988**, *36*, 1261–1270. [CrossRef]
9. Evans, W.J. Creep-fatigue Interactions in Ti-6Al-4V at ambient temperatures. In Proceedings of the Third International Conference on Creep and Fracture of Eng Materials and Structures, Swansea, UK, 5–10 April 1987; Evans, W.J., Ed.; pp. 603–613.
10. Venkatesh, V.; Noraas, R.; Pilchak, A.; Tamirisa, S.; Calvert, K.; Salem, A.; Broderick, T.; Glavicic, M.G.; Saraf, V. Data Driven Tools and Methods for Microtexture Classification and Dwell Fatigue Life Prediction in Dual Phase Titanium Alloys. *MATEC Web Conf.* **2020**, *321*, 11091. [CrossRef]
11. Li, J.; Davies, H.M.; Fox, K.; Mulyadi, M.; Glavicic, M.G.; Bache, M.R. An appraisal of dwell sensitive fatigue in Ti-6Al-4V and the governing role of inhomogeneous micro-texture. *Int. J. Fatigue* **2023**, *171*, 107589. [CrossRef]

12. Woodfield, A.P.; Gorman, M.D.; Sutliff, J.A.; Corderman, R.R. Effect of microstructure on dwell fatigue behavior of Ti-6242. In *Ti' 95 Science and Technology, Proceedings of the Eighth World Conference on Titanium, Birmingham, UK, 22–26 October 1995*; Blenkinsop, P.A., Evans, W.J., Flower, H.M., Eds.; IOM: Birmingham, UK, 1996.
13. Rugg, D.; Dixon, M.; Dunne, F.P.E. Effective structural unit size in titanium alloys. *J. Strain Anal. Eng. Des.* **2007**, *42*, 269–279. [CrossRef]
14. Pilchak, A.L.; Shank, J.; Tucker, J.C.; Srivatsa, S.; Fagin, P.N.; Semiatin, S.L. A dataset for the development, verification, and validation of microstructure-sensitive process models for near-alpha titanium alloys. *Integr. Mater. Manuf. Innov.* **2016**, *5*, 259–276. [CrossRef]
15. Germain, L.; Gey, N.; Humbert, M.; Vo, P.; Jahazi, M.; Bocher, P. Texture heterogeneities induced by subtransus processing of near α titanium alloys. *Acta Mater.* **2008**, *56*, 4298–4308. [CrossRef]
16. Pilchak, A.; Fox, K.; Payton, E.; Wiedemann, M.; Broderick, T.; Delaleau, P.; Michael, G.; Nigel, J.; Jean-Manuel, R.; Brian, S.; et al. *Cold Dwell Fatigue of Titanium Alloys: History, Current State, and Aviation Industry Perspective*; United States Department of Transportation: Washington, DC, USA; Federal Aviation Administration: Washington, DC, USA; William J. Hughes Technical Center: Atlantic City, NJ, USA, 2024.
17. Dunne, F.P.E.; Rugg, D.; Walker, A. Lengthscale-dependent, elastically anisotropic, physically-based hcp crystal plasticity: Application to cold-dwell fatigue in Ti alloys. *Int. J. Plast.* **2007**, *23*, 1061–1083. [CrossRef]
18. Bache, M.R.; Davies, H.M.; Evans, W.J. A Model for Fatigue Crack Initiation in Titanium Alloys. In Proceedings of the Eighth World Conference on Titanium, Birmingham, UK, 22–26 October 1995; Blenkinsop, P.A., Evans, W.J., Flower, H.M., Eds.; IOM: Birmingham, UK, 1996; pp. 1347–1354.
19. Bache, M.R.; Cope, M.; Davies, H.M.; Evans, W.J.; Harrison, G. Dwell sensitive fatigue in a near alpha titanium alloy at ambient temperature. *Int. J. Fatigue* **1997**, *19*, 83–88. [CrossRef]
20. Kassner, M.E.; Kosaka, Y.; Hall, J.A. Low-Cycle Dwell-Time Fatigue in Ti-6242. *Metall. Mater. Trans. A* **1999**, *30*, 2383–2389. [CrossRef]
21. Bache, M.; Germain, L.; Jackson, T.; Walker, A.R.M. Mechanical and Texture Evaluations of Ti 6246 as a Dwell Fatigue Tolerant Alloy. In Proceedings of the 11th World Conference on Titanium, Kyoto, Japan, 3–7 June 2007.
22. Davey, W.; Bache, M.R.; Davies, H.M.; Thomas, M.; Bermant-Parr, I. Fatigue Performance of the Novel Titanium Alloy TIMETAL® 407. *MATEC Web Conf.* **2020**, *321*, 11044. [CrossRef]
23. Bache, M.; Davies, H.; Davey, W.; Thomas, M.; Berment-Parr, I. Microstructural control of fatigue behaviour in a novel α + β titanium alloy. *Metals* **2019**, *9*, 1200. [CrossRef]
24. Thomas, M.; Hewitt, J.; Bache, M.; Thomas, R.; Garratt, P.; Kosaka, Y. Determination and Analysis of the Cyclic and Dwell Fatigue Performance of Timetal® 575. In Proceedings of the 13th World Conference on Titanium; John Wiley & Sons: Hoboken, NJ, USA, 2016; pp. 979–984.
25. Hewitt, J.S.; Davies, P.D.; Thomas, M.J.; Garratt, P.; Bache, M.R. Titanium alloy developments for aeroengine fan systems. *Mater. Sci. Technol.* **2014**, *30*, 1919–1924. [CrossRef]
26. Wu, Z.; Kou, H.; Chen, N.; Xi, Z.; Fan, J.; Tang, B.; Li, J. Recent developments in cold dwell fatigue of titanium alloys for aero-engine applications: A review. *J. Mater. Res. Technol.* **2022**, *20*, 469–484. [CrossRef]
27. Rolls-Royce plc. TITANIUM ALLOY AND METHOD OF MANUFACTURE. European Patent EP4640859A1, 29 October 2025. Available online: https://eur03.safelinks.protection.outlook.com/?url=https%3A%2F%2Fworldwide.espacenet.com%2Fpatent%2Fsearch%2Ffamily%2F091275161%2Fpublication%2FEP4640859A1%3Fq%3DEP4640859A1&data=05%7C02%7CP.D.Davies%40swansea.ac.uk%7C24826e24e8be41b9fa8208de27726605%7Cbbcab52e9fbe43d6a2f39f66c43df268%7C0%7C0%7C638991569452551717%7CUnknown%7CTWFpbGZsb3d8eyJFbXB0eU1hcGkiOnRydWUsIlYiOiIwLjAuMDAwMCIsIlAiOiJXaW4zMiIsIkFOIjoiTWFpbCIsIldUIjoyfQ%3D%3D%7C0%7C%7C%7C%7C&sdata=sgJsg4%2BSZWcHYW6As3fJnWYEIRCDYYC8OBERNxBzHJE%3D&reserved=0 (accessed on 1 August 2025).
28. Lister, S.; Baxter, G.J.; Jackson, M. Titanium-S23: A New Alloy with Ultra-High Tensile Toughness Directly from the Solid-State Processing of Recycled Ti–6Al–4V and Ti–5Al–5Mo–5V–3Cr Powders using Field Assisted Sintering Technology. *Adv. Eng. Mater.* **2025**, *27*, 2500572. [CrossRef]
29. Wagner, V.; Baili, M.; Dessein, G. The relationship between the cutting speed, tool wear, and chip formation during Ti-5553 dry cutting. *Int. J. Adv. Manuf. Technol.* **2015**, *76*, 893–912. [CrossRef]
30. *BS EN 2002-1:2005*; Aerospace Series. Metallic Materials. Test Methods—Tensile Testing at Room Temperature. British Standards Institution (BSI): London, UK, 2005.
31. *ISO 1099:2017*; Metallic Materials—Fatigue Testing—Axial force—Controlled Method. International Organization for Standardization: Geneva, Switzerland, 2017.
32. Properties and Processing of TIMETAL 6-4, TIMET Brochure. Available online: https://www.timet.com/assets/local/documents/technicalmanuals/TIMETAL_6-4_Properties.pdf (accessed on 1 August 2025).

33. Bache, M.R.; Li, J.; Davies, H.M. A re-assessment of Ti-685 as a dwell sensitive titanium alloy and a definition for engineering relevant dwell behaviour. *Int. J. Fatigue* **2024**, *178*, 108008. [CrossRef]
34. Bantounas, I.; Dye, D.; Lindley, T.C. The role of microtexture on the faceted fracture morphology in Ti-6Al-4V subjected to high-cycle fatigue. *Acta Mater.* **2010**, *58*, 3908–3918. [CrossRef]
35. Pilchak, A.L.; Hutson, A.; Porter, W.J.; Buchanan, D.; John, R. On the Cyclic Fatigue and Dwell Fatigue Crack Growth Response of Ti-6Al-4V. In Proceedings of the 13th World Conference on Titanium; Wiley: Hoboken, NJ, USA, 2016; pp. 993–998. [CrossRef]
36. Lavogiez, C.; Dureau, C.; Nadot, Y.; Villechaise, P.; Hémery, S. Crack initiation mechanisms in Ti-6Al-4V subjected to cold dwell-fatigue, low-cycle fatigue and high-cycle fatigue loadings. *Acta Mater.* **2023**, *244*, 118560. [CrossRef]
37. Rolls-Royce/ISM Swansea unpublished data. 2025.